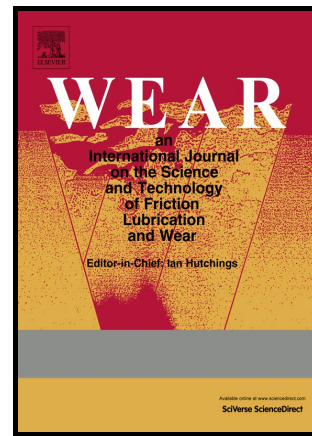


## Author's Accepted Manuscript

The effect of sub-models and parameterizations in the simulation of abrasive jet impingement tests

Gianandrea Vittorio Messa, Stefano Malavasi



PII: S0043-1648(16)30569-5  
DOI: <http://dx.doi.org/10.1016/j.wear.2016.10.022>  
Reference: WEA101813

To appear in: *Wear*

Received date: 4 August 2016  
Revised date: 4 October 2016  
Accepted date: 27 October 2016

Cite this article as: Gianandrea Vittorio Messa and Stefano Malavasi, The effect of sub-models and parameterizations in the simulation of abrasive jet impingement tests, *Wear*, <http://dx.doi.org/10.1016/j.wear.2016.10.022>

This is a PDF file of an unedited manuscript that has been accepted for publication. As a service to our customers we are providing this early version of the manuscript. The manuscript will undergo copyediting, typesetting, and a review of the resulting galley proof before it is published in its final citable form. Please note that during the production process errors may be discovered which could affect the content, and all legal disclaimers that apply to the journal pertain.

# The effect of sub-models and parameterizations in the simulation of abrasive jet impingement tests

Gianandrea Vittorio Messa\*, Stefano Malavasi

*DICA, Politecnico di Milano, Piazza Leonardo da Vinci, 32 20133 Milano, Italy*

---

## Abstract

Since experimental erosion testing is rarely feasible in the engineering practice, the estimate of erosion is often performed by numerical simulations. Computational Fluid Dynamics (CFD) codes are often equipped with utilities for wear estimation which rely on a well-established methodology. However, besides requiring stringent assumptions, this methodology involves a number of sub-models and parameterizations which, being difficult to define a priori, are potential sources of uncertainty. The objective of this work is to investigate how the erosion estimates are affected by the different sub-models and parameters of a CFD-based wear prediction model, so that its actual predictive capacity may be established. We referred to the benchmark case of the abrasive jet impingement test which, despite being widely studied both experimentally and numerically, highlights all the issues of impact erosion modelling. A systematic activity of simulation of previous experiments revealed the key role played by some fluid-dynamics related quantities, such as the formulation of the particle equation of motion, besides the erosion model.

---

\*Corresponding author

*Email addresses:* [gianandreavittorio.messa@polimi.it](mailto:gianandreavittorio.messa@polimi.it) (Gianandrea Vittorio Messa), [stefano.malavasi@polimi.it](mailto:stefano.malavasi@polimi.it) (Stefano Malavasi)

Moreover, it allowed providing guidelines for increasing the reliability of the estimates.

*Keywords:* abrasive jet testing; computational fluid dynamics; impact wear; slurry erosion.

---

## 1. Introduction

It is well known that impact erosion is a very serious concern in the oil and gas industry due to the considerable economic damages related to this phenomenon [1].

A procedure for the prediction of erosion based on Computational Fluid Dynamics (CFD) simulations is well-established since the 1990s, and it involves two steps in sequence, namely simulation of the fluid-particle flow by a two-phase model based on the Eulerian-Lagrangian approach [2] (in which the fluid flow is solved in an Eulerian framework and the solid phase is simulated by tracking the trajectories of a certain number of particles), and application of a single-particle erosion model. The single-particle erosion models, which in large numbers have been proposed in the literature [3, 4], are mostly empirical or semi-empirical algebraic correlations which express the mass of material removed by a particle hitting a surface,  $E_p$ , as a function of several parameters, including the particle mass,  $m_p$ , the modulus of the particle velocity at the impact stage,  $|\mathbf{v}_{p,w}|$ , the particle impingement angle,  $\theta_{w,p}$ , some particle-related characteristics, such as its size and shape, and some mechanical properties of the target material, such as its hardness (Fig. 1). Hereafter, we will denote as “Erosion Prediction Model” (EPM) the combination of the Eulerian-Lagrangian fluid-dynamic model and the erosion

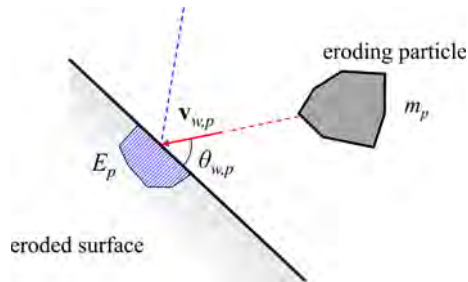


Figure 1: An eroding particle hitting a surface

model.

At present, guaranteeing the reliability of the wear estimates is difficult due to the large number of submodels and parameters of the EPM, which are illustrated in Fig. 2. These include several items related to the Eulerian-Lagrangian calculations, as well as the used erosion model and the values of all its coefficients. It is worth noticing that the elements in Fig. 2 are unlikely to be defined by theoretical considerations or consistency analyses, because they are essentially empirical or semi-empirical and, furthermore, they depend upon parameters of uncertain nature or difficult to quantify. Other well known limitations of CFD-based erosion prediction, which won't be considered in this paper, are the high computational cost of the Eulerian-Lagrangian models, which makes it difficult to address flows with moderate and high solid content [5, 6], and the neglect of the self-induced geometry changes due to erosion, which may prevent the possibility of attaining reliable long-term erosion estimates [7–9].

In this analysis, reference is made to the benchmark case of the impingement of an abrasive jet against a specimen (Fig. 3). Experimental tests on this equipment have been the subject of several papers, in which the erosion

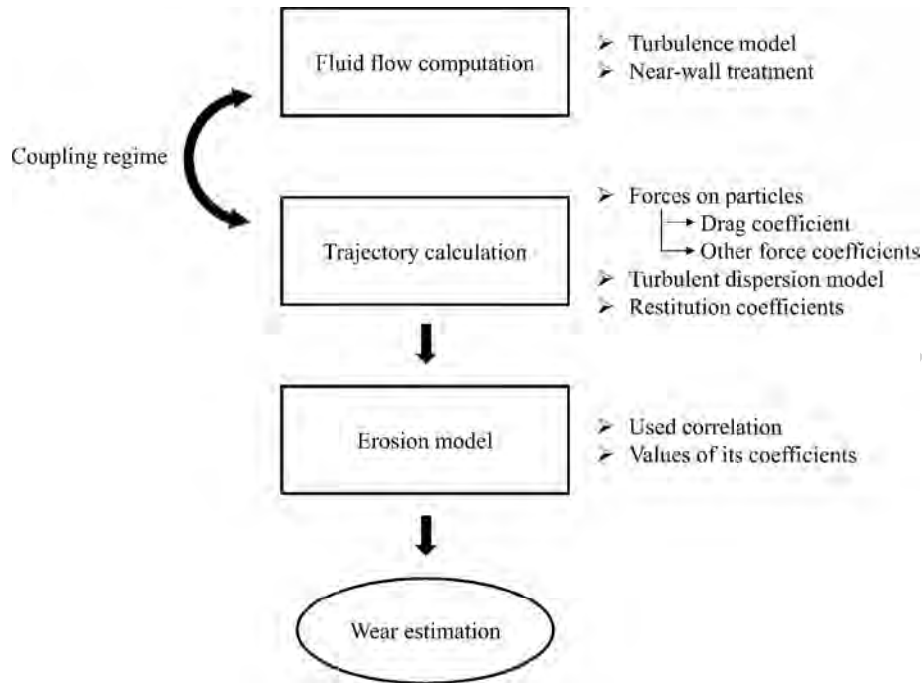


Figure 2: Sub-models and parameters of the EPM

was typically quantified by means of the integral erosion ratio,  $ER_{\text{int}}$ , that is the ratio between the mass loss of the specimen and the mass of solids come out from the nozzle. In fewer studies [9–18], the authors provided also data on the erosion scar. Difficulties exist in the experimental evaluation of erosion even under the relatively controlled conditions allowed by the abrasive jet test rig, and the complex issue of evaluating the uncertainty of experimental data has been addressed in a limited number of researches, such as Arabnejad et al. [19].

Abrasive jet impingement tests have been numerically reproduced by many researchers [9–13, 15, 16, 20–25] who, in the end, were always capable to attain good agreement between CFD predictions and some experimen-

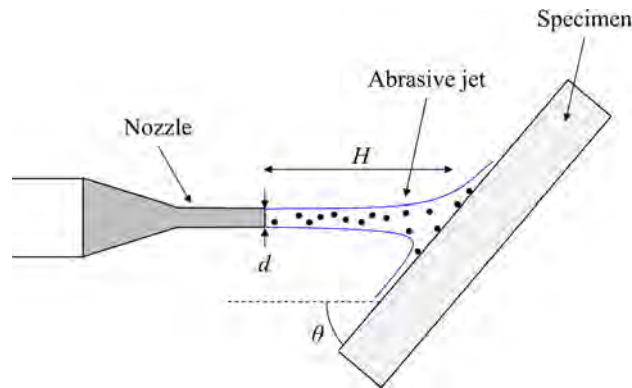


Figure 3: Sketch of an abrasive jet impingement test

tal measurements. However, establishing the real predictive capability of the EPMs employed in these studies is difficult because, besides the erosion model, also all other sub-models and parameters are very different, and its has been never clarified up to which extent these items affect the erosion estimates.

This is the objective of the present paper. After a careful screening of the pertinent literature, we numerically reproduced thirteen experiments of abrasive jet tests, carried out by different authors [10, 12, 21, 23] and judged the most significant for the present analysis. Particularly, we focused on tests in which the carrier fluid is a liquid since the broader range of impact angles and velocities involved compared to air-solid flows allows more meaningful testing of the capabilities of CFD-base predictive methods. We carefully analyzed the effect of the potential sources of uncertainty of the EPM, listed in Fig. 2, in order to find the parameters which most influence the erosion estimate and, after assessing their effect on the results, discuss the level of accuracy currently allowed by these methods.

As a final note, we might add that, even if our research is aimed at the oil and gas industry, the benchmark case considered in this study is significant for a variety of engineering applications. A significant example is the use of abrasive waterjet for either cutting or polishing surfaces, which have also been the subject of CFD-based investigations [26–30]. Even if the specific findings of this study may not be valid in other contexts, the fundamental message of this investigation it is. That is, addressing the issue of the robustness of the wear estimates obtained by an EPM as a fundamental step for establishing its real predictive capacity.

The remainder of this paper is divided in two sections, followed by the conclusions. In Section 2, the mathematical model is described, together with the numerical setup and the computational methodology. In Section 3, the obtained results are illustrated and discussed.

## 2. Mathematical model

### 2.1. Governing equations

As it will be demonstrated at the beginning of Section 3, for the case studies under consideration a one-way coupled model provides roughly the same results as a two-way coupled one. As a consequence, almost all the simulations have been performed under the assumption of one-way coupling regime, thereby decoupling the fluid flow computation from the tracking of the particles. The fluid flow field has been obtained by solving the RANS equations for single-phase flow, in conjunction with a turbulence model for evaluating the Reynolds stresses [31]. Particularly, three turbulence models have been tested to analyze the sensitivity of the wear estimates upon

this parameter, namely the  $k$ - $\omega$  SST turbulence model [32], the standard  $k - \varepsilon$  model for high Reynolds flows in conjunction with the standard wall function [33], and the  $k - \varepsilon$  RNG model [34] in conjunction with the non-equilibrium wall function [35]. Solution of these equations yields the mean velocity vector of the fluid,  $\mathbf{U}$ , the mean pressure,  $P$ , the turbulent kinetic energy of the fluid,  $k$ , the specific dissipation,  $\omega$  (possibly replaced by the turbulent dissipation rate,  $\varepsilon$ ). In the two-way coupled simulations, source terms accounting for the effect of the solids on the fluid have been included in the momentum equations for the fluid phase.

The liquid-solid flow field has been simulated in the framework of the point-particle approximation, i.e. by treating the particles as mathematical point sources of momentum. The Lagrangian tracking calculations are performed by solving the equation of motion for each particle. Unlike almost all previous studies, which considered simplified expressions after claiming the minor importance of the neglected terms, here we refer to a more general formulation of the particle equation of motion, taken from Loth [36], in order to assess the relevance of the different contributions. The following equation

$$\begin{aligned}
 (\rho_p + c_v \rho_f) W_p \frac{d\mathbf{v}_p}{dt} = & -\frac{1}{8} \pi \rho_f d_p^2 C_d |\mathbf{w}| \mathbf{w} + \\
 (\rho_p - \rho_f) W_p \mathbf{g} + \rho_f W_p \left( c_v \frac{d\mathbf{u}_{@p}}{dt} + \frac{D\mathbf{u}_{@p}}{Dt} \right) + & \quad (1) \\
 J^* \cdot 3.0844 \frac{m_p}{\rho_p d_p} \sqrt{\frac{\nu}{|\boldsymbol{\omega}|}} (\boldsymbol{\omega} \times \mathbf{w}) &
 \end{aligned}$$

is solved in conjunction with another ordinary differential equation for particle position,

$$\frac{d\mathbf{x}_p}{dt} = \mathbf{v}_p \quad (2)$$

Eq. 1 states that the rate of change of the particle linear momentum is equal

to the sum of the forces acting on it, which are the gravitational force, the fluid stress force (including buoyancy), the added mass force, and the lift force. The symbols in Eqs. 1 and 2 are as follows:  $\rho_f$  and  $\rho_p$  are the densities of the fluid and the solid particles, respectively;  $\nu$  is the kinematic viscosity coefficient of the fluid;  $W_p$  is the particle volume;  $\mathbf{x}_p$  is the particle position vector;  $\mathbf{v}_p$  is the instantaneous particle velocity vector;  $\mathbf{u}_{@p}$  is the instantaneous unhindered fluid velocity vector, i.e. the fluid-phase velocity that can be hypothetically extrapolated to the particle center of mass;  $\mathbf{w}$  is the relative velocity vector of the particle, equal to  $\mathbf{u}_{@p} - \mathbf{v}_p$ ;  $d_p$  is the equivalent volumetric diameter of a particle;  $\mathbf{g}$  is the gravitational acceleration vector; and  $\boldsymbol{\omega}$  is the unhindered fluid vorticity. The operators  $d/dt$  and  $D/Dt$  are the particle-path and fluid-path Lagrangian time derivatives, defined along a path specified by  $\mathbf{v}_p$  and  $\mathbf{u}$ , respectively. The coefficients  $C_d$ ,  $c_v$ , and  $J^*$  are associated to the drag force, the added mass force, and the lift force, as it will be discussed below. The history force has not been included because the flows considered in this study are characterized by relatively high particle Reynolds numbers  $\text{Re}_p = |\mathbf{w}|d_p/\nu$  and, therefore, it can be regarded as negligible [36].

The drag coefficient,  $C_d$ , has been evaluated by the following correlation, developed by Haider and Levenspiel [37], which allows accounting for the effect of particle shape:

$$C_d = \frac{24}{\text{Re}_p} (1 + A\text{Re}_p^B) + \frac{C}{1 + D/\text{Re}_p} \quad (3)$$

where  $\text{Re}_p$  is the already mentioned particle Reynolds number, and  $A$ ,  $B$ ,  $C$ ,

and  $D$  are numerical coefficients defined as follows:

$$A = \exp(2.33 - 6.46\phi + 2.45\phi^2) \quad (4a)$$

$$B = 0.096 + 0.557\phi \quad (4b)$$

$$C = \exp(4.91 - 13.89\phi + 18.42\phi^2 - 10.26\phi^3) \quad (4c)$$

$$D = \exp(1.47 + 12.26\phi - 20.37\phi^2 + 15.89\phi^3) \quad (4d)$$

in which  $\phi$  is the particle spherical coefficient, i.e. the ratio between the surface area of a sphere having the same volume of the considered particle and the actual surface area of the particle.

The virtual mass coefficient,  $c_v$ , has been set to 0.5 as commonly used in the literature.

The term  $J^*$  has been empirically introduced by Mei [38] to extend the lift force formula developed by Saffman to finite  $Re_p$ . The expression for  $J^*$  is

$$J^* = \begin{cases} (1 - 0.3314\sqrt{\alpha}) \exp\left(-\frac{Re_p}{10}\right) + 0.3314\sqrt{\alpha}, & \text{if } Re_p \leq 40 \\ 0.0524\sqrt{\alpha Re_p}, & \text{if } Re_p > 40 \end{cases} \quad (5)$$

where:

$$\alpha = \frac{\sqrt{2\mathbf{D} : \mathbf{D}}}{|\mathbf{w}|} d_p \quad (6)$$

being  $\mathbf{D}$  the strain rate tensor of the fluid.

The instantaneous velocity of the fluid,  $\mathbf{u}$ , is obtained by a well-established “discrete random walk” stochastic model [39], which is the most frequently employed in similar studies.

Finally, we underline that, even if the point-particle approximation has been invoked, the finite size of the particles has been indirectly accounted for

by evaluating the particle impingement characteristics at a distance from the solid wall equal to the particle radius.

## 2.2. Erosion models

As it has already been discussed, the erosion model must be included among the parameters which potentially affect the wear estimates. In order to quantify this effect, use is made of different erosion models, which have been selected among those available in the literature in considerations of their widespread use and applicability.

### 2.2.1. The Oka erosion model

The empirical model developed by Oka, Okamura, and Yoshida [40, 41], which is referred to as Oka in this study, is one of the most comprehensive from the point of view of the number of independent parameters and, also for this reason, it is one of the most commonly used. The equation for  $E_p$  is:

$$E_p = 10^{-9} m_p \rho_w K H_\nu^{k_1} \left( \frac{|\mathbf{v}_{w,p}|}{V'} \right)^{k_2} \left( \frac{d_p}{D'} \right)^{k_3} f(\theta_{w,p}) \quad (7)$$

$$f(\theta_{w,p}) = (\sin \theta_{w,p})^{n_1} [1 + H_\nu (1 - \sin \theta_{w,p})^{n_2}] \quad (8)$$

where  $\rho_w$  is the density of the target material,  $V'$  and  $D'$  are a reference particle velocity and a reference particle size, equal to 104 m/s and 326  $\mu\text{m}$ , respectively,  $H_\nu$  is the Vickers number of the target material, and  $k_2$ ,  $n_1$ , and  $n_2$  are equal to  $2.3H_\nu^{0.038}$ ,  $s_1 H_\nu^{q_1}$ , and  $s_2 H_\nu^{q_2}$ , respectively. The values of the numerical coefficients employed in this study, which were obtained by best-fit of experiments with silica particles, are as follows:  $K = 65$ ,  $k_1 = -0.112$ ,  $k_3 = 0.19$ ,  $s_1 = 0.71$ ,  $s_2 = 2.4$ ,  $q_1 = 0.14$ , and  $q_2 = -0.94$ .

### 2.2.2. The E/CRC mechanistic erosion model

A mechanistic erosion model has been recently developed by the Erosion/Corrosion Research Center (E/CRC) of the University of Tulsa, which is based on two erosion mechanisms, namely cutting erosion and deformation erosion [42]. The formula for  $E_p$  is:

$$E_p = F_s \rho_w \frac{CW_C + W_D}{m_p} \quad (9)$$

where  $F_s$  is a particle shape coefficient,  $C$  is the cutting erosion constant, and  $W_C$  and  $W_D$  are the volume removed by cutting and deformation, respectively. These quantities are calculated as follows:

$$W_C = \begin{cases} \frac{m_p |\mathbf{v}_{w,p}|^{2.41} (K \sin 2\theta_{w,p} - \sin^2 \theta_{w,p})}{2K^2 P^*}, & \text{if } \theta_{w,p} \leq \tan^{-1} K \\ \frac{m_p |\mathbf{v}_{w,p}|^{2.41} \cos^2 \theta_{w,p}}{2P}, & \text{if } \theta_{w,p} > \tan^{-1} K \end{cases} \quad (10)$$

$$W_D = \frac{1}{2} \frac{m_p (|\mathbf{v}_{w,p}| \sin \theta_{w,p} - U_{tsh})^2}{\epsilon} \quad (11)$$

where  $K$  is the ratio of vertical to horizontal force component on a particle,  $P^*$  is the flow pressure for annealed material which is assumed to be equal to its Vickers hardness,  $U_{tsh}$  is the threshold velocity below which deformation wear is negligible, and  $\epsilon$  is the deformation wear factor. The empirical constants of this models, which have been determined for several materials by best-fit of experimental data, are  $F_s$ ,  $C$ ,  $K$ ,  $U_{tsh}$ , and  $\epsilon$ . Particularly,  $F_s$  and  $K$  depend upon the shape of the particles ( $F_s = 1$  for fully sharp particles, 0.53 for semi-rounded particles, 0.20 for fully rounded particles; and  $K$  ranging from 0.4 to 1 according to the angularity of the particles),  $U_{tsh}$  on the target material and the particle size, and  $C$  and  $K$  on the target material.

### 2.2.3. The DNV-GL erosion model

The DNV-GL equation [43] have been worked out based on experimental investigations available in literature, dedicated erosion tests and experience and models available within the company. This is of considerable relevance in the oil and gas sector, and takes the following form:

$$E_p = K |\mathbf{v}_{w,p}|^n f(\theta_{w,p}) m_p \quad (12)$$

The model is applicable to quartz sand with semi-rounded or angular shape. Recommended values of the empirical parameters  $K$  and  $n$  are provided for the most commonly-used materials. For a variety of steel grades, including those of our parametric study,  $K = 2.0 \cdot 10^{-9} [\text{m/s}]^{-n}$  and  $n = 2.6$ . For aluminium,  $K = 5.8 \cdot 10^{-9} [\text{m/s}]^{-n}$  and  $n = 2.3$ . For all ductile materials, the impact angle function is given by:

$$f(\theta_{w,p}) = A [\sin \theta_{w,p} + B (\sin \theta_{w,p} - \sin^2 \theta_{w,p})]^k \cdot [1 - \exp(-C\theta_{w,p})] \quad (13)$$

where  $A = 0.6$ ,  $B = 7.2$ ,  $C = 20$ , and  $k = 0.6$ .

### 2.2.4. The Huang erosion model

Also the phenomenological model developed by Huang et al. [44], here referred to as Huang model, involves cutting and deformation erosion mechanisms. The expression actually used arises from a simplification of a more general formulation, theoretically comprehensive but difficult to apply in practice. The final formula is

$$E_p = 10^{-9} m_p \rho_w D d_p^{0.5} \rho_p^{0.1875} |\mathbf{v}_{w,p}|^{2.375} \cos^2 \theta_{w,p} \cdot \sin^{0.375} \theta_{w,p} + 10^{-9} m_p \rho_w C \rho_p^{0.15} (|\mathbf{v}_{w,p}| \sin \theta_{w,p})^{2.3} \quad (14)$$

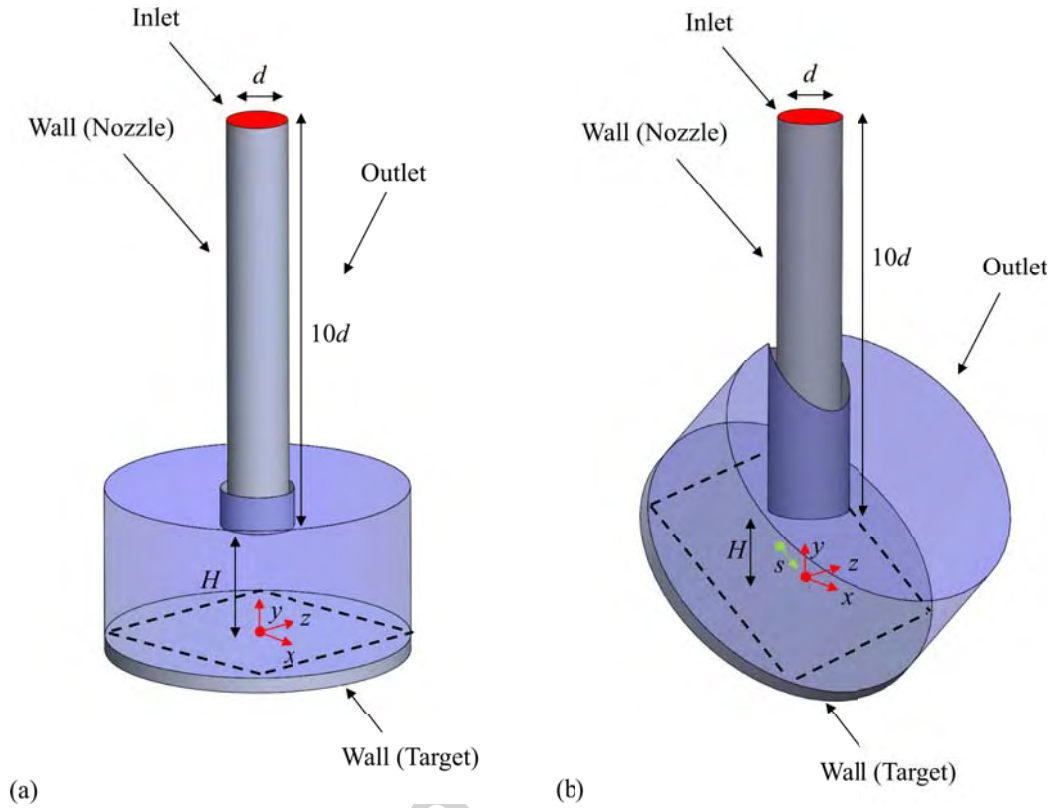


Figure 4: Computational domain and boundary conditions for normal jet (a) and inclined jet (b)

where  $D = 0.082$  and  $C = 7.5 \cdot 10^{-4}$  for SAE-1055 steel. The dimensions of  $d_p$ ,  $\rho_p$ ,  $m_p$ , and  $|\mathbf{v}_{w,p}|$  are [m], [ $\text{kg}/\text{m}^3$ ], [kg], and [m/s], respectively.

### 2.3. Computational domain and boundary conditions

Both normal and inclined impinging jets have been considered in this study. Figures 4(a) and (b) show the computational domain and the boundary conditions (which are inlet, outlet, and solid walls) for the two cases. The lower boundary is a circle which circumscribes the target specimen used in

the experiments, which from case to case was square, rectangular (as qualitatively depicted using a dotted line) or circular. The nozzle has been modeled as a straight pipe with length equal to 10 diameters, as this type of representation is adequate for simulating the experiments of interest for this study. It is clear, however, that the model is no longer appropriate when different nozzle geometries result in more complex interactions between the jet flow and the inside nozzle wall.

A fully-developed flow profile is specified at the inlet sections, with the distributions of the mean axial fluid velocity, turbulent kinetic energy, and dissipation rate determined from Nikuradse's boundary layer theory [45] for single-phase flow in straight pipes.

$$\begin{aligned}
 U_n^{\text{in}} = |\mathbf{U}^{\text{in}}| &= U \frac{(N+1)(2N+1)}{2N^2} \left(1 - \frac{2r}{d}\right)^{1/N} \\
 N &= \frac{1}{\sqrt{f}} \quad f = \left[ \frac{1}{1.82 \log(\text{Re}_b) - 1.64} \right]^2 \\
 k^{\text{in}} &= U^2 \frac{f}{8} \left[ 1 + \frac{2}{3} \frac{2r}{d} + \frac{10}{3} \left(\frac{2r}{d}\right)^3 \right] \\
 \omega^{\text{in}} &= C_\mu^{3/4} \frac{(k^{\text{in}})^{1/2}}{l_m} \\
 l_m &= \frac{d}{2} \left[ 0.14 - 0.08 \frac{2r}{d} - 0.06 \left(\frac{2r}{d}\right)^4 \right]
 \end{aligned} \tag{15}$$

In the equation above,  $U$  is the bulk-mean jet velocity,  $r$  is the local distance from the nozzle axis,  $N$  and  $C_\mu = 0.09$  are dimensionless coefficients,  $f$  is the friction factor,  $l_m$  is the mixing length, and  $\text{Re}_b$  is a bulk Reynolds number defined with respect to  $U$ ,  $d$ , and  $\nu$ . When employing the  $k - \varepsilon$  standard and RNG turbulence models, the turbulent dissipation rate at the inlet section,

$\varepsilon^{\text{in}}$ , was calculated as  $\omega^{\text{in}}k^{\text{in}}$ . No mean relative velocity is assumed between the phases at the inlet boundary. That is, the particle velocities at the inlet section,  $\mathbf{v}_p^{\text{in}}$ , are equal to the mean fluid velocity plus a fluctuation, as follows,

$$\mathbf{v}_p^{\text{in}} = \mathbf{U}_{@p}^{\text{in}} + \boldsymbol{\xi} \sqrt{\frac{2k_{@p}^{\text{in}}}{3}} \quad (16)$$

where  $\boldsymbol{\xi}$  is a three-element vector containing random scalars drawn from the standard PDF. The initial particle positions are determined by imposing the local particle number density to be proportional to the local advective fluid mass flux per unit area, i.e.  $\rho_f U_{n@p}^{\text{in}}$ . All particles are attributed the same mass flux, which is determined in such a way that the total solid mass flux equals the desired value.

At the outlet boundaries the mean pressure is specified and held constant to a zero value. The particles simply leave the domain.

At the solid walls, no slip is assumed for the fluid phase. The fluid wall shear stress and the values of the turbulent parameters in the near-wall cells were evaluated in different ways, according to the used turbulence model. When employing the  $k - \omega$  model, these quantities are obtained from the standard option available in the used code [39]. Conversely, when employing the  $k - \varepsilon$  standard and the  $k - \varepsilon$  RNG models, the fluid wall shear stress, the turbulent kinetic energy, and the turbulent dissipation rate close to the wall have been calculated by means of the already mentioned standard and non-equilibrium wall functions. The normal and tangential particle velocities are related to the corresponding incident values via two restitution coefficients, referred to as  $e_n$  and  $e_t$ , which are usually expressed as a function of the impact angle,  $\theta_{w,p}$ . Since, as already shown in Fig. 2,  $e_n$  and  $e_t$  are potential

sources of uncertainty in wear estimation, use is made of two couples of expressions relating these parameters to  $\theta_{w,p}$ . The former consists of the formulas developed by Forder, Thew, and Harrison [46], reported below.

$$e_n = 0.988 - 0.78\theta_{w,p} + 0.19\theta_{w,p}^2 - 0.024\theta_{w,p}^3 + 0.027\theta_{w,p}^4 \quad (17a)$$

$$e_t = 1 - 0.78\theta_{w,p} + 0.84\theta_{w,p}^2 - 0.21\theta_{w,p}^3 + 0.028\theta_{w,p}^4 - 0.022\theta_{w,p}^5 \quad (17b)$$

The latter is an analogous set of equations proposed by Grant and Tabakoff [47], as follows,

$$e_n = 0.988 - 1.66\theta_{w,p} + 2.11\theta_{w,p}^2 + 0.67\theta_{w,p}^3 \quad (18a)$$

$$e_t = 0.993 - 1.76\theta_{w,p} + 1.56\theta_{w,p}^2 - 0.49\theta_{w,p}^3 \quad (18b)$$

Finally, wear predictions have also been carried out by setting both restitution coefficients equal to a unit value, which represents the ideal condition of perfectly elastic particle-wall collisions.

#### 2.4. Computational methodology and consistency of the numerical solution

The mathematical model described above was implemented in the ANSYS FLUENT software version 17 using the User-Defined Functions, and the code was employed to perform the numerical calculations. The RANS equations have been discretized using the finite volume method, and the Second Order Upwind scheme [39] is used to discretize the transport equations. The finite volume equations are solved iteratively by means of the SIMPLE algorithm [39]. The under-relaxation factors correspond to the default settings in ANSYS FLUENT.

The tracking of the particle trajectories is performed by means of the Discrete Phase Model embedded in the FLUENT code. The particle equations

of motion (Eq. 1) are integrated over a timestep obtained from a length scale of 1 mm. The second order implicit Runge-Kutta method [39] is used for time stepping.

Extensive MATLAB routines have been developed for estimating the erosion starting from the particle characteristics at the impact stage produced as output by FLUENT. Particularly, the wall boundaries have been triangulated using enough triangles to produce consistent wear predictions. Each impact point has been associated to the centroid of the nearest triangle. Application of the erosion model (Sub-section 2.2) in which the particle mass  $m_p$  is replaced by the particle mass flux  $\dot{m}_p$ , and the particle impact velocity and angle are evaluated at a distance from the wall equal to the particle radius, yields the mass flux of eroded material removed by the current particle. The sum of over the particles hitting the same triangle gives the erosion rate of this element, that is  $\dot{E}_{tr}$  [kg/s]. Finally, the integral erosion ratio,  $ER_{int}$  [kg/kg], has been obtained by summing the  $\dot{E}_{tr}$  values over the elements and dividing by the solid mass flux entering the domain through the inlet section. The erosion depth of each triangle at time  $t$ ,  $\eta_{tr,t}$ , is evaluated as:

$$\eta_{tr,t} = \frac{\dot{E}_{tr}}{A_{tr}\rho_w}t \quad (19)$$

where  $A_{tr}$  is the area of the triangle.

The consistency of the numerical solution with respect to the number grid elements used to discretize the flow domain,  $N_{el}$ , and the number of tracked particles,  $N_p$ , is proved. Even under the one-way coupling assumption, the number of grid elements used for solving the RANS can influence the wear estimates by affecting the numerical integration of Eq. 1. On the other side,

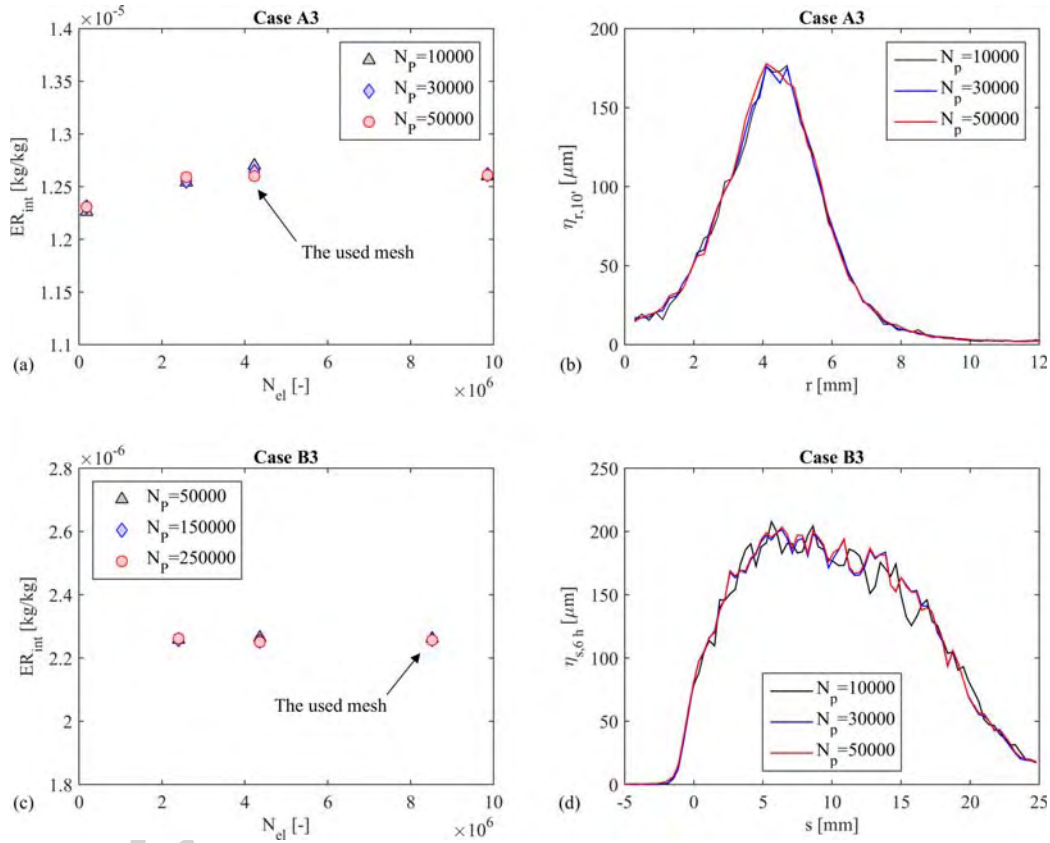


Figure 5: Consistency analysis of the erosion predictions with respect to the number of grid elements and number of tracked particles. Results for cases A3 (a,b) and B3 (c,d).

since the erosion at the wall due to the individual particle impacts is related to the mass flux  $\dot{m}_p$  that each particle represents, it is necessary to ensure that a statistically representative set of particle impingements is obtained.

The analysis has been performed for all the simulated scenarios, and the results will be shown for a couple of them, referred to as cases A3 and B3 in Table 1, where the geometrical and flow conditions are reported. In these simulations, the submodels and parameters of the EPM were as follows: one-way coupling between fluid and particle;  $k-\omega$  SST turbulence model; particle equation of motion as in Eq. 1, including turbulent dispersion; Haider and Levenspiel drag coefficient correlation (Eq. 3) with  $\phi = 0.76$ ; Forder, Thew, and Harrison correlations for the restitution coefficients (Eq. 17); Oka erosion model (Eq. 7). The mesh was made of tetrahedral cells, densified close to the intersection between the nozzle axis and the specimen, and surface inflation is used in the proximity of the wall boundaries.

Four different meshes, consisting of about 0.3, 1.0, 4.7, and 10 million elements were employed for case A3. For each mesh, the number of tracked particles was increased from 10000 to 50000. Figure 5(a) shows the predicted integral erosion ratio,  $ER_{\text{int}}$ , as a function of the number of grid elements for different amounts of tracked particles, and it reveals a relatively stable behavior. As it will be shown afterward, the scar caused by a normal jet is essentially axi-symmetrical with respect to the nozzle axis and, therefore, it can be characterized by the radial erosion depth profile (obtained by circumferential averaging the local values). Figure 5(b) shows the estimated scar profile after 10 minutes of exposure to wear (referred to as  $\eta_{r,10'}$ ) as obtained on the finest mesh for different values of  $N_p$ . The plots reveal that  $N_p$  has a

more qualitative than quantitative effect on the erosion depth profile, which requires  $N_p$  to be equal to 30000 for becoming relatively smooth. Based on these results, in all the normal jet impingement simulations use is made of a mesh consisting of about 4 million elements and 30000 particles were tracked.

Figure 5(c) is the analog of Fig. 5(a) for case B3. In this case, the three meshes were made of 2.4, 4.3, and 8.5 million cells, and the tracked particles were 50000, 150000, and 250000. Even if the effect of  $N_{el}$  and  $N_p$  on the integral erosion ratio was minor, Fig. 5(d) shows that a considerable number of particles was needed to partially reduce the oscillations in the wear profile after 6 hours testing along the axis of the specimen (coordinate  $s$  in Fig. 4b). This is due to the fact that, unlike the radial depth profile of the normal jet cases, only a small fraction of the impacts contributes to the scar along the axis; therefore, in order to attain a stable profile, much more particles have to be tracked. Finally, we decided to make use of the 8.5 million cells mesh and release 150000 particles.

### 3. Results and discussion

The influence of the sub-models and parameters of the EPM listed in Fig. 2 have been studied. This has been done by simulating six experiments performed by Nguyen et al. [10] and Mansouri et al. [20], in which both the integral erosion ratio and the shape of the eroded profile are provided, and the maximum scar depth is sufficiently low ( $< 150 \mu\text{m}$ ) for the geometry changes due to erosion to be regarded as negligible, at least as a first approximation. These cases are referred to as A1 to B3 in Table 1, which reports the details of the testing conditions. Additional experiments in which only the integral

| Case | Ref. | $d$ [mm] | $U$ [m/s] | $\theta$ [°] | Target                            | Particles     | $\rho_p$ [kg/m <sup>3</sup> ] | $d_p$ [ $\mu$ m] | C [%] | Testing time |
|------|------|----------|-----------|--------------|-----------------------------------|---------------|-------------------------------|------------------|-------|--------------|
| A1   |      |          |           |              | SUS304                            |               |                               | 50               |       |              |
| A2   | [10] | 6.4      | 30        | 90           | $\rho_w = 7929$ kg/m <sup>3</sup> | Corundum      | 3940                          | 80               | 0.5   | 10 min       |
| A3   |      |          |           |              | $H_v = 1.96$ GPa                  |               |                               | 150              |       |              |
| B1   |      |          |           |              | SS316                             | Oklahoma #1   |                               | 150              |       |              |
| B2   | [20] | 8        | 14        | 90           | $\rho_w = 8000$ kg/m <sup>3</sup> | California 60 | 2650                          | 300              | 0.6   | 6 h          |
| B3   |      |          |           |              | $H_v = 2.24$ GPa                  | California 60 |                               | 300              |       |              |
| C1   |      |          |           |              | Inconel 625                       | Oklahoma #1   |                               | 150              |       |              |
| C2   |      |          |           |              | $\rho_w = 8200$ kg/m <sup>3</sup> | Oklahoma #1   |                               | 150              |       |              |
| C3   | [21] | 8        | 2.5       | 90           | $H_v = 3.43$ GPa                  | Oklahoma #1   | 2650                          | 150              | 0.5   | $\approx$ h  |
| C4   |      |          |           |              |                                   | Silica Flour  |                               | 25               |       |              |
| D1   |      |          |           |              | Al 6061-T6                        | California 60 |                               | 300              |       |              |
| D2   | [23] | 8        | 10        | 90           | $\rho_w = 2700$ kg/m <sup>3</sup> | Oklahoma #1   | 2650                          | 150              | 0.1   | N.A.         |
| D3   |      |          |           |              | $H_v = 1.12$ GPa                  | Silica Flour  |                               | 20               |       |              |

Table 1: Flow conditions considered in the parametric study. For all cases, the nozzle-to-specimen distance,  $H$ , is equal to 12.7 mm

erosion ratio were provided, conducted by Zhang et al. [21] and Okita et al. [23], have been numerically reproduced. For these cases, labeled as C1 to D3, the parametric study was limited to the effect of the erosion correlation, which, as it will be shown, plays a very important role.

The remainder of this section is divided in five sub-sections in which, after showing the typically obtained solutions for normal and inclined jets, the effect of the coupling regime and the model for the fluid phase, the correlation for the restitution coefficients, the formulation of the particle equation of motion, and the erosion model are investigated.

### *3.1. Typically obtained solutions*

The flow characteristics of impinging jets have been extensively studied and they are well documented in the literature. As an example, Figures 6(a-d) represent the color plot distribution and the mean pressure of a perpendicular jet (case A3) and an inclined one (case B3) on the half-mid plane of the computational domain, as obtained from single-phase flow simulations using the  $k - \omega$  SST turbulence model. The fluid leaving the nozzle rapidly decelerates in the proximity of the target; after impingement, it radially deflects in the perpendicular case (Fig. 6(a)), whilst it tends to slide down the specimen in the inclined one (Fig. 6(b)). The fluid deceleration is accompanied by an increase in its mean pressure, which reaches the maximum value in correspondence to the stagnation point (Fig. 6(c,d)). Figures 6(e,f) show the erosion depth distributions at the end of the test as obtained with the same numerical settings of the consistency analysis described in Sub-section 2.4. As already noticed, in the perpendicular case the axisymmetrical shape of the scar (Fig. 6(e)) allows its representation by means of the radial profile.

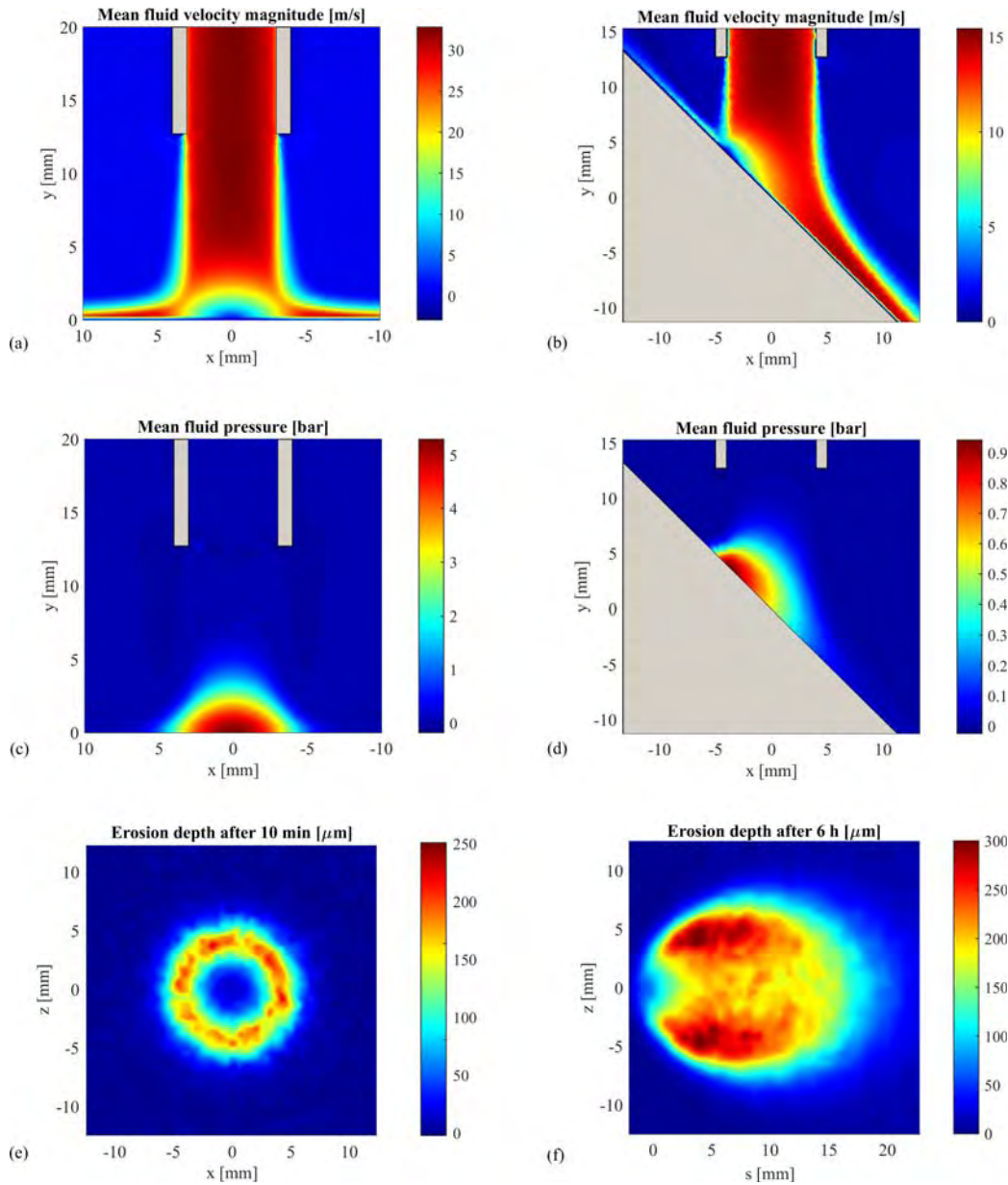


Figure 6: Numerical solution of cases A3 (a,c,e) and B3 (b,d,f). Color plots of the mean velocity magnitude of the fluid (a,b), the mean pressure of the fluid (c,d), and of the erosion depth at the end of the test (e,f)

| Coupling regime | Fluid phase closures                  | $ER_{\text{int}}$ [kg/kg] |
|-----------------|---------------------------------------|---------------------------|
| one-way         | $k - \omega$ SST                      | $1.26 \cdot 10^{-5}$      |
| two-way         | $k - \omega$ SST                      | $1.25 \cdot 10^{-5}$      |
| one-way         | $k - \varepsilon$ RNG + non eq. w.f.  | $1.25 \cdot 10^{-5}$      |
| one-way         | $k - \varepsilon$ standard + eq. w.f. | $1.28 \cdot 10^{-5}$      |

Table 2: Effect of the coupling regime and of the CFD closures for the fluid phase on the integral erosion ratio for case A3

Conversely, the scar is symmetrical with respect to the  $s$  axis in the inclined case (Fig. 6(f)). The erosion depth profile along  $s$  has been measured by Mansouri et al. [20].

### 3.2. Effect of the coupling regime and the closures for the fluid phase

At first, we focused on the coupling regime between the two phases and the fluid-dynamic closures for the carrier fluid (turbulence model and wall treatment). The study has been performed for case A3, keeping the other items of the EPM the same as in the consistency analysis.

Since previous investigations show differences in the definition of the coupling regime when the solid volume fraction is about 0.5%, we compared the wear estimates obtained by one-way and two-way coupled models using the  $k - \omega$  SST turbulence model. Since the obtained predictions are substantially coincident in terms of both erosion depth profile and integral erosion ratio (Fig. 7(a) and Table 2), we run all other simulations under the assumption of one-way coupling regime.

Similarly, changes in the turbulence model and the type of near-wall treatment produce minor variations in the predicted integral erosion ratio

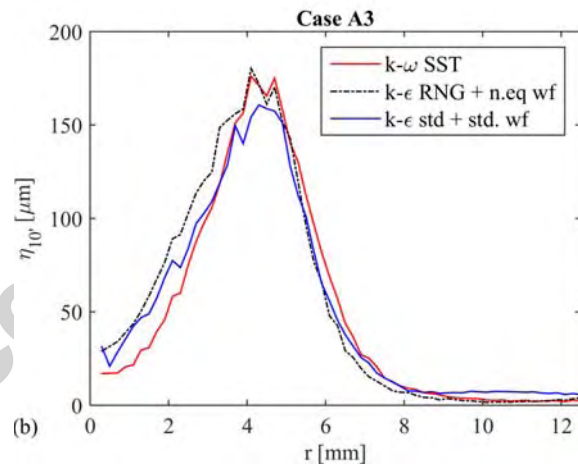
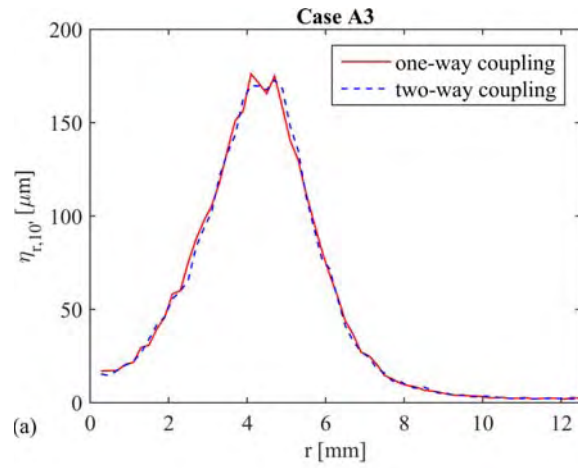


Figure 7: Effect of the coupling regime (a) and of the CFD closures for the fluid phase (b) on the erosion depth profile for case A3

| Restitution coefficients | $ER_{\text{int}}$ [kg/kg] |                      |
|--------------------------|---------------------------|----------------------|
|                          | Case A3                   | Case B3              |
| Forder et al.            | $1.26 \cdot 10^{-5}$      | $2.26 \cdot 10^{-6}$ |
| Grant and Tabakoff       | $1.25 \cdot 10^{-5}$      | $2.24 \cdot 10^{-6}$ |
| Perfectly elastic        | $1.30 \cdot 10^{-5}$      | $2.26 \cdot 10^{-6}$ |

Table 3: Effect of the model for the restitution coefficients on the integral erosion ratio for cases A3 and B3

(Table 2), and have a moderate effect on the scar profile (Fig. 7(b)). From this point onwards, the  $k - \omega$  SST turbulence model is used.

### 3.3. Effect of the model for the restitution coefficients

As a second step, we investigated the effect of the model for restitution coefficients. The options considered in addition to the Forder, Thew, and Harrison correlations (Eq. 17) are the Grant and Tabakoff formulas (Eq. 18), and the perfectly elastic collision model, in which both restitution coefficients are attributed a unit value. The analysis, which have been carried out for cases A1 to B3 with the usual other EPM settings, indicated that the chosen model for the restitution coefficients (and even the extremely simplifying assumption that no energy loss occurs after a collision) has a minor influence on the wear prediction. This is exemplified in Fig. 8 and Table 3 for cases A3 and B3. The Forder, Thew, and Harrison formulas [46] have been employed in the remainder of the simulations.

### 3.4. Effect of the particle equation of motion

The study was performed starting from the general formulation of the particle equation of motion proposed by Loth [36] and illustrated in Sub-

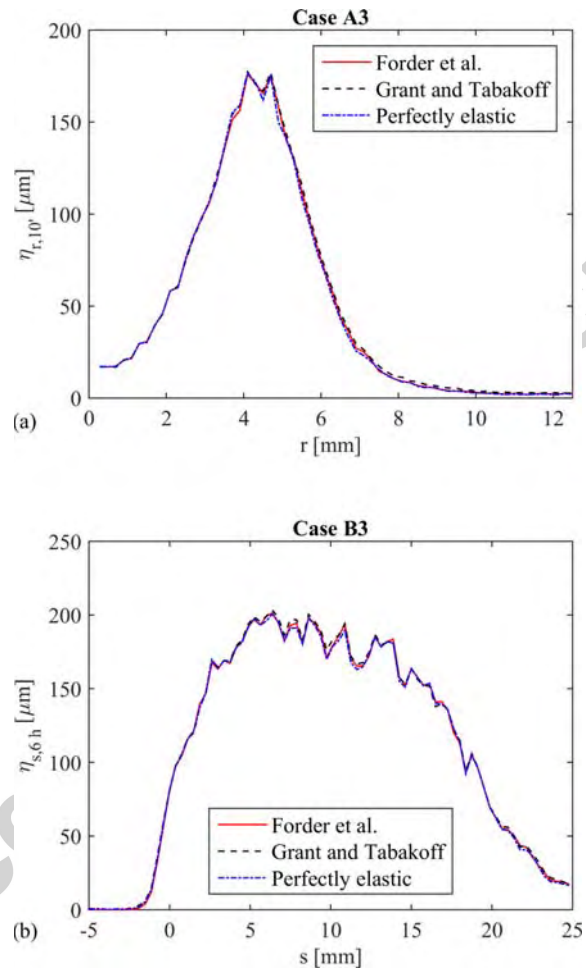


Figure 8: Effect of the model for the restitution coefficients on the erosion depth profile for cases A3 (a) and B3 (b)

section 2.1.

As a first step, we established which are the forces acting on the particle which must be accounted for and those which can be neglected. As Fig. 9 and Table 4 show, neglecting the gravitational force, the buoyancy, and the added mass force produces minor changes in the wear estimate. The lift force appears substantially negligible for all cases but A1, in which the particles are very small ( $50 \mu\text{m}$ ). Conversely, the fluid stress force plays a very important role, probably due to the high pressure gradient that occurs close to the stagnation point. In the same way, also turbulent dispersion was found to be of considerable importance. Based on these results, in the rest of the simulations we neglected gravity, buoyancy, and added mass, and we accounted for the lift force only for the finest particles (cases A1 and C4).

As a second step, we focused on the effect of the particle spherical coefficient,  $\phi$ , in the Haider and Levenspiel drag coefficient correlation (Eq. 3). Even if  $\phi$  has a precise geometric meaning, assigning a numerical value to this parameter is hard in practice, also for controlled laboratory tests. The handbook by W.C. Yang [48] indicates the sphericity of sharp and round sand particles to be 0.66 and 0.86, respectively. This range was considered in the sensitivity analysis, in addition with the ideal case of spherical particles ( $\phi = 1$ ). As usual, wear has been estimated by the Oka erosion model. Figure 10 and Table 5 highlight the important role played by  $\phi$  in affecting the erosion predictions. In all cases, an increase in  $\phi$  causes an increase in the predicted maximum depth of wear scar and, generally, a reduction of its extension. Conversely, no unique trend exists for the integral erosion ratio.

Accounting for the role played by  $\phi$  in the configuration of the particle tra-

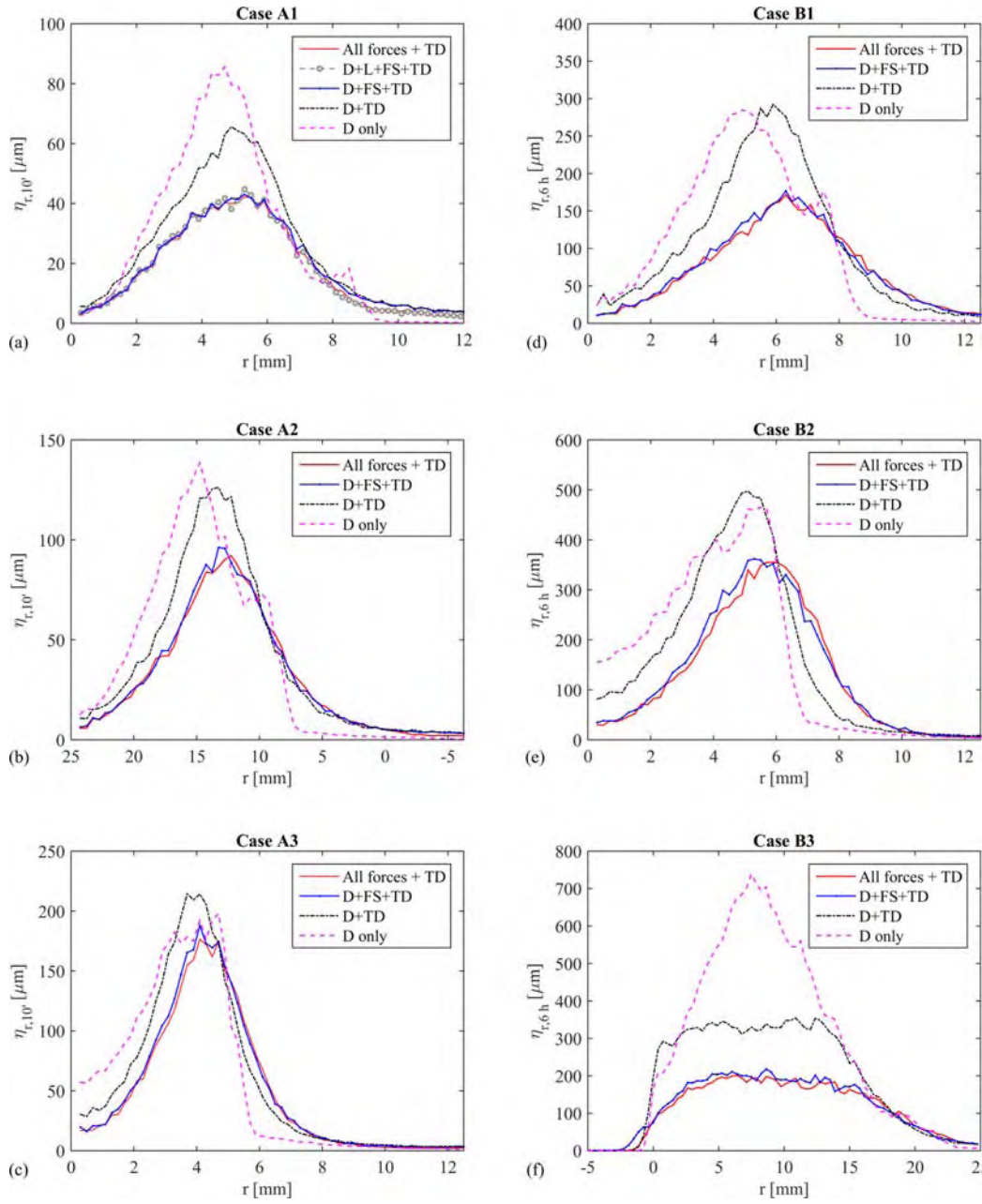


Figure 9: Effect of the terms in the particle equation of motion on the erosion depth profile for cases A1 to B3. Acronyms are as follows: D=drag force included; L=lift force included; FS=fluid stress force included; TD=turbulent dispersion accounted for

| Particle equation of motion | $ER_{\text{int}}$ [kg/kg] |                      |                      |                      |                      |                      |
|-----------------------------|---------------------------|----------------------|----------------------|----------------------|----------------------|----------------------|
|                             | Case A1                   | Case A2              | Case A3              | Case B1              | Case B2              | Case B3              |
| All forces + TD             | $5.39 \cdot 10^{-6}$      | $9.03 \cdot 10^{-6}$ | $1.26 \cdot 10^{-5}$ | $1.60 \cdot 10^{-6}$ | $2.36 \cdot 10^{-6}$ | $2.26 \cdot 10^{-6}$ |
| D + L + FS + TD             | $5.37 \cdot 10^{-6}$      |                      |                      |                      |                      |                      |
| D + FS + TD                 | $5.94 \cdot 10^{-6}$      | $9.26 \cdot 10^{-6}$ | $1.30 \cdot 10^{-5}$ | $1.61 \cdot 10^{-6}$ | $2.42 \cdot 10^{-6}$ | $2.27 \cdot 10^{-6}$ |
| D + TD                      | $7.45 \cdot 10^{-6}$      | $1.08 \cdot 10^{-5}$ | $1.36 \cdot 10^{-5}$ | $2.05 \cdot 10^{-6}$ | $2.57 \cdot 10^{-6}$ | $3.02 \cdot 10^{-6}$ |
| D                           | $6.98 \cdot 10^{-6}$      | $9.24 \cdot 10^{-6}$ | $1.15 \cdot 10^{-5}$ | $1.70 \cdot 10^{-6}$ | $2.17 \cdot 10^{-6}$ | $3.15 \cdot 10^{-6}$ |

Table 4: Effect of the terms in the particle equation of motion for cases A1 to B3. Acronyms are as in Fig. 9

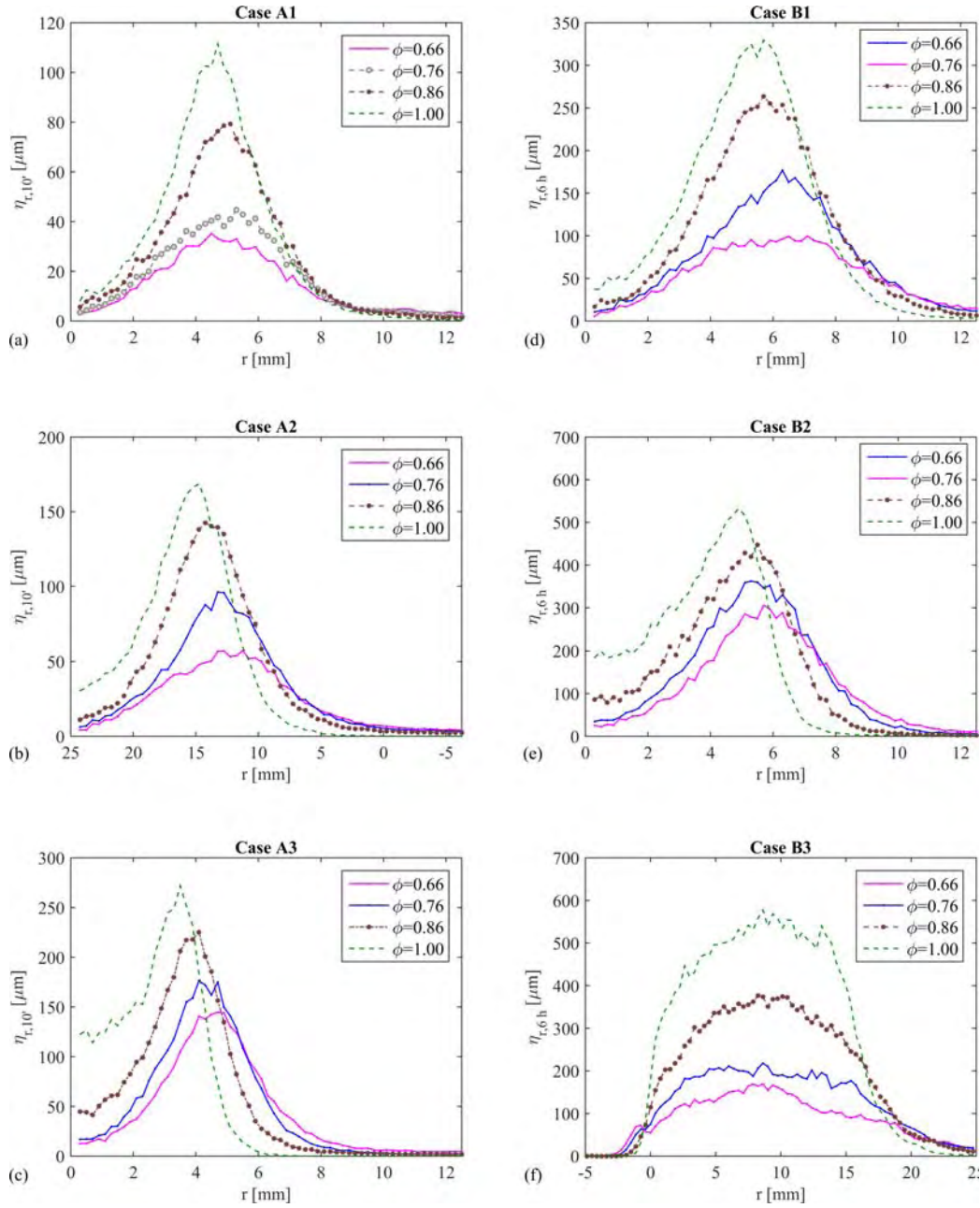


Figure 10: Effect of the particle spherical coefficient in the Haider and Levenspiel drag coefficient correlation (Eq. 3) for cases A1 to B3.

| $\phi$ | $E_{\text{int}}^{\text{num}}$ [kg/kg] |                      |                      |                      |                      |                      |
|--------|---------------------------------------|----------------------|----------------------|----------------------|----------------------|----------------------|
|        | Case A1                               | Case A2              | Case A3              | Case B1              | Case B2              | Case B3              |
| 0.66   | $4.55 \cdot 10^{-6}$                  | $7.45 \cdot 10^{-6}$ | $1.26 \cdot 10^{-5}$ | $1.23 \cdot 10^{-6}$ | $2.28 \cdot 10^{-6}$ | $1.82 \cdot 10^{-6}$ |
| 0.76   | $5.37 \cdot 10^{-6}$                  | $9.26 \cdot 10^{-6}$ | $1.30 \cdot 10^{-5}$ | $1.61 \cdot 10^{-6}$ | $2.42 \cdot 10^{-6}$ | $2.27 \cdot 10^{-6}$ |
| 0.86   | $7.46 \cdot 10^{-6}$                  | $1.08 \cdot 10^{-5}$ | $1.20 \cdot 10^{-5}$ | $1.95 \cdot 10^{-6}$ | $2.30 \cdot 10^{-6}$ | $2.82 \cdot 10^{-6}$ |
| 1.00   | $8.20 \cdot 10^{-6}$                  | $9.18 \cdot 10^{-6}$ | $1.01 \cdot 10^{-5}$ | $2.02 \cdot 10^{-6}$ | $2.06 \cdot 10^{-6}$ | $3.41 \cdot 10^{-6}$ |

Table 5: Effect of the particle spherical coefficient in the Haider and Levenspiel drag coefficient correlation (Eq. 3) for cases A1 to B3

jectories may partially help in providing a physical justification to the results. Compared to particles with low  $\phi$ , particles with high  $\phi$  are characterized by lower drag coefficient and, therefore, they are more inertia-dominated. As a consequence, the impact velocity is higher and the deflection of the trajectories leaving the nozzle is less pronounced, resulting in impact angles closer to the nozzle-to-specimen one. This seems the basis behind the different shapes of the wear scar in the perpendicular jets. Nevertheless, it appears very difficult to provide full interpretation of these results, as other issues emerge due to the facts that the relation between  $E_p$  and  $\theta_{w,p}$  is not monotonic for ductile materials and that erosion depends also on the number of impingements.

In summary, the value of the particle spherical coefficient,  $\phi$ , is an important uncertainty factor of the EPM. For cases A1 to B3, a change in  $\phi$  between 0.66 and 0.86 causes variations up to about 3 and 2 in terms of maximum erosion depth and integral erosion ratio, respectively. Therefore, employing a drag correlation for spherical particles in case of non-spherical abrasives can lead to significant inaccuracies.

|         | $\phi$ | $F_s$ | $C$     | $K$ | $U_{tsh}$ [m/s] | $\epsilon$ [kg/m · s <sup>2</sup> ] |
|---------|--------|-------|---------|-----|-----------------|-------------------------------------|
| Case A1 | 0.66   | 1.00  | 0.01260 | 0.4 | 30.55           | $1.47 \cdot 10^{11}$                |
| Case A2 | 0.66   | 1.00  | 0.01260 | 0.4 | 15.09           | $1.47 \cdot 10^{11}$                |
| Case A3 | 0.66   | 1.00  | 0.01260 | 0.4 | 5.88            | $1.47 \cdot 10^{11}$                |
| Case B1 | 0.76   | 0.53  | 0.01260 | 0.4 | 5.88            | $1.47 \cdot 10^{11}$                |
| Case B2 | 0.66   | 1.00  | 0.01260 | 0.4 | 2.00            | $1.47 \cdot 10^{11}$                |
| Case B3 | 0.66   | 1.00  | 0.01260 | 0.4 | 2.00            | $1.47 \cdot 10^{11}$                |
| Case C1 | 0.76   | 0.53  | 0.01340 | 0.4 | 3.91            | $2.72 \cdot 10^{11}$                |
| Case C2 | 0.76   | 0.53  | 0.01340 | 0.4 | 3.91            | $2.72 \cdot 10^{11}$                |
| Case C3 | 0.76   | 0.53  | 0.01340 | 0.4 | 3.91            | $2.72 \cdot 10^{11}$                |
| Case C4 | 0.66   | 1.00  | 0.01340 | 0.4 | 57.46           | $2.72 \cdot 10^{11}$                |
| Case D1 | 0.66   | 1.00  | 0.00436 | 0.4 | 2.57            | $6.53 \cdot 10^{10}$                |
| Case D2 | 0.76   | 0.53  | 0.00436 | 0.4 | 7.28            | $6.53 \cdot 10^{10}$                |
| Case D3 | 0.66   | 1.00  | 0.00436 | 0.4 | 149.52          | $6.53 \cdot 10^{10}$                |

Table 6: Values of  $\phi$  and parameters of the E/CRC model for all the testing conditions

### 3.5. Effect of the erosion model

Finally, the effect of the erosion model has been investigated, focusing on the four correlations reported in Sub-section 2.2. For each testing condition, the mechanical properties of the target material are defined in Table 1. Significant effort has been devoted to properly define the particle spherical coefficient. Following an established classification from the E/CRC, we divided the particles into fully sharp, semi-rounded, and fully rounded, characterized by  $\phi$  equal to 0.66, 0.76, and 0.86, respectively. The assignment of a class to each case was done on the basis of the information reported in the related papers, and the  $\phi$  values are reported in Table 6. The E/CRC model requires knowledge of the constants  $F_s$ ,  $C$ ,  $K$ ,  $U_{tsh}$ ,  $\epsilon$ , which are actually dif-

|         | $ER_{\text{int}}$ [kg/kg] |                      |                      |                      |                      |
|---------|---------------------------|----------------------|----------------------|----------------------|----------------------|
|         | Oka                       | E/CRC                | DNV-GL               | Huang                | Exp.                 |
| Case A1 | $4.55 \cdot 10^{-6}$      | $1.33 \cdot 10^{-5}$ | $1.63 \cdot 10^{-6}$ | $1.19 \cdot 10^{-5}$ | $6.73 \cdot 10^{-6}$ |
| Case A2 | $7.45 \cdot 10^{-6}$      | $2.01 \cdot 10^{-5}$ | $2.56 \cdot 10^{-6}$ | $2.17 \cdot 10^{-5}$ | $1.50 \cdot 10^{-5}$ |
| Case A3 | $1.26 \cdot 10^{-5}$      | $3.09 \cdot 10^{-5}$ | $4.67 \cdot 10^{-6}$ | $3.77 \cdot 10^{-5}$ | $1.98 \cdot 10^{-5}$ |
| Case B1 | $1.61 \cdot 10^{-6}$      | $1.93 \cdot 10^{-6}$ | $4.98 \cdot 10^{-7}$ | $5.21 \cdot 10^{-6}$ | $9.46 \cdot 10^{-7}$ |
| Case B2 | $2.28 \cdot 10^{-6}$      | $4.54 \cdot 10^{-6}$ | $6.94 \cdot 10^{-7}$ | $8.10 \cdot 10^{-6}$ | $1.57 \cdot 10^{-6}$ |
| Case B3 | $1.82 \cdot 10^{-6}$      | $3.62 \cdot 10^{-6}$ | $5.17 \cdot 10^{-7}$ | $6.93 \cdot 10^{-6}$ | $1.48 \cdot 10^{-6}$ |
| Case C1 | $5.11 \cdot 10^{-7}$      | $5.77 \cdot 10^{-7}$ | $2.02 \cdot 10^{-7}$ | $2.13 \cdot 10^{-6}$ | $9.30 \cdot 10^{-8}$ |
| Case C2 | $9.06 \cdot 10^{-8}$      | $1.02 \cdot 10^{-7}$ | $3.15 \cdot 10^{-8}$ | $3.86 \cdot 10^{-7}$ | $1.80 \cdot 10^{-8}$ |
| Case C3 | $1.33 \cdot 10^{-8}$      | $1.49 \cdot 10^{-8}$ | $4.00 \cdot 10^{-9}$ | $5.87 \cdot 10^{-8}$ | $1.30 \cdot 10^{-9}$ |
| Case C4 | $1.54 \cdot 10^{-8}$      | $4.62 \cdot 10^{-8}$ | $6.89 \cdot 10^{-9}$ | $4.71 \cdot 10^{-8}$ | $3.40 \cdot 10^{-8}$ |
| Case D1 | $5.49 \cdot 10^{-7}$      | $4.88 \cdot 10^{-7}$ | $4.67 \cdot 10^{-7}$ | $1.30 \cdot 10^{-6}$ | $3.21 \cdot 10^{-6}$ |
| Case D2 | $4.03 \cdot 10^{-7}$      | $2.09 \cdot 10^{-7}$ | $3.32 \cdot 10^{-7}$ | $8.32 \cdot 10^{-7}$ | $1.46 \cdot 10^{-6}$ |
| Case D3 | $4.55 \cdot 10^{-8}$      | $5.66 \cdot 10^{-8}$ | $3.91 \cdot 10^{-8}$ | $5.48 \cdot 10^{-8}$ | $9.78 \cdot 10^{-8}$ |

Table 7: Integral erosion ratio of all test cases: numerical predictions using different erosion models versus experimental data [10, 12, 21, 23]

difficult to set. The values listed in Table 6 have been chosen on the grounds of the data and criteria reported in [42], possibly referring to the more similar material. In the DNV equation, the  $K$  and  $n$  values for steel grades have been employed for all cases but D1 to D3, where those recommended for aluminium have been set.

The high variability induced by the erosion model selection is evident in Figs. 11 and 12 and Table 7. None of the four tested correlations is capable in achieving accurate predictions for all conditions. The Oka erosion model produces the best overall predictive performance, in terms of both scar profile and integral erosion ratio. The E/CRC mechanistic model tends to overes-

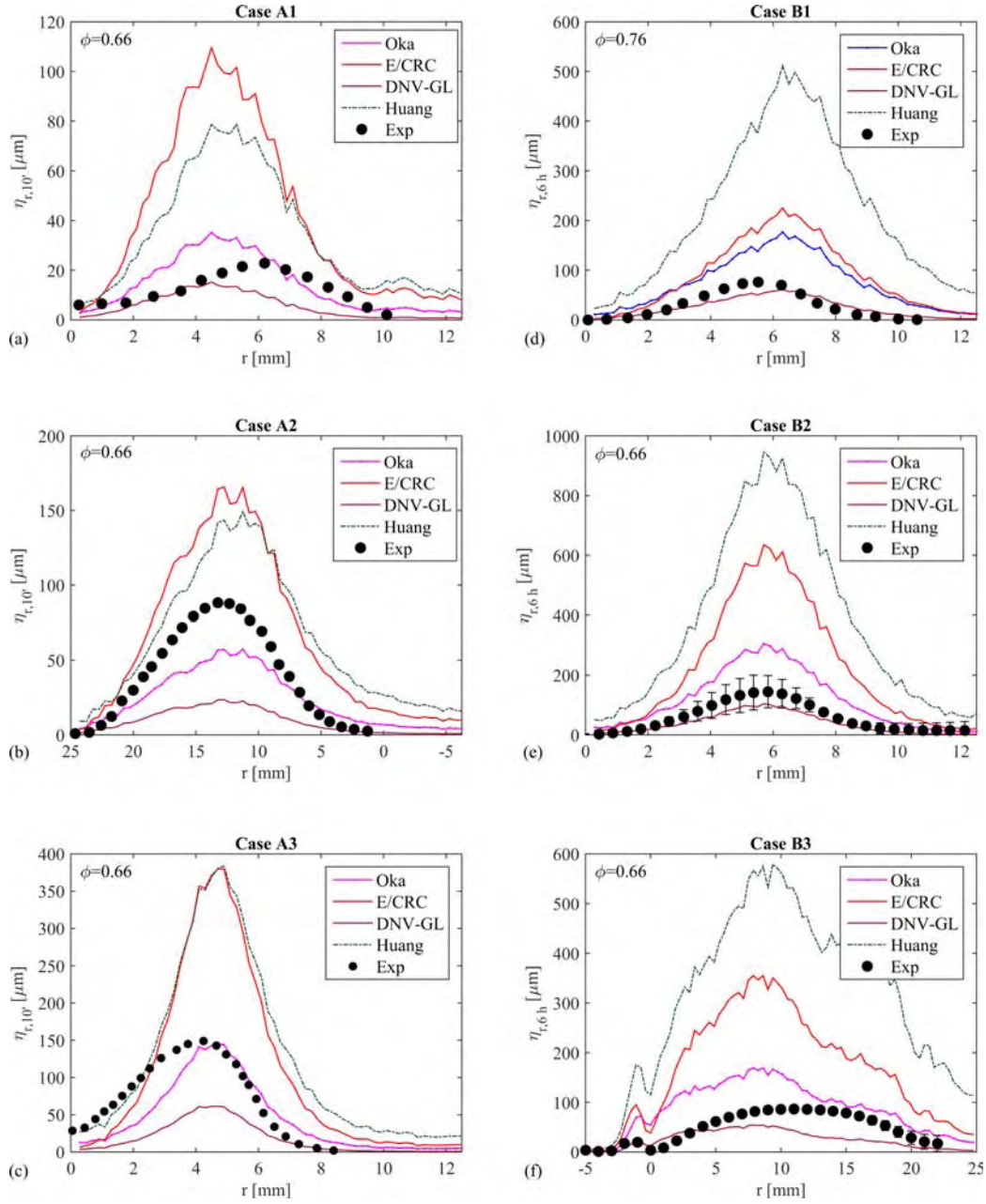


Figure 11: Scar profile at the end of the test for cases A1 to B3: numerical predictions using different erosion models versus experimental data [10, 12]

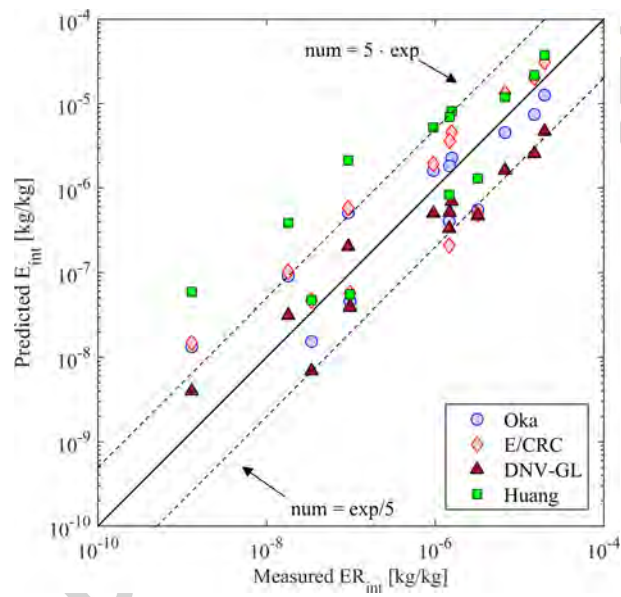


Figure 12: Log-log parity plot of measured integral erosion ratio versus numerical prediction obtained using different erosion models for all cases

timate the experimental data, in some cases even significantly. However, it should be noted that this model has considerable inherent variability due to parameters which are very hard to set, such as  $C$ ,  $U_{tsh}$ , and  $\epsilon$ . Conversely, the DNV-GL correlation is simpler, but it strongly underestimates the measured erosion. Instead, the Huang model is likely to overestimate the data.

The above results suggest that the Oka model provides the greatest possibility to attain reasonable estimates. Moreover, one of the strengths of this model is that the mechanical properties of the target material required as input are its density and Vickers number, which are generally known. However, deviations in the integral erosion ratio are expected up to a factor of 5, and this seems the maximum level of accuracy allowed by CFD-based erosion prediction methods at present. Much effort is required to deepen into the physical mechanisms of particle flow and impact erosion, in order to increase the reliability of the models.

#### 4. Conclusion

Starting from the observation of the considerable differences in the CFD-based Erosion Prediction Models (EPM) which have been used for reproducing abrasive jet impingement tests in previous investigations, we carried out a systematic analysis aimed at identifying the sub-models and parameters of the EPM which most affect the wear estimates and pointing out the level of accuracy currently allowed by this approach. This has been done by thinking of abrasive jet impingement tests as the first step before addressing more complex flows of interest in the oil and gas industry.

This work showed that the reliability of the EPM cannot prescind from the

consistency of the fluid dynamic model, with regard to both fluid flow computation and particle tracking. After proving that two-phase jets with solid volume fractions around 0.5% can be modeled as one-way coupled (Fig. 7(a) and Table 2), we found that the wear predictions are not a strong function of the turbulence closures (Fig. 7(b) and Table 2) and that the values of the restitution coefficients play a minor role (Fig. 8 and Table 3).

Conversely, it is fundamental to properly define the particle equation of motion: the fluid stress force plays an important role due to the high pressure gradient which occurs close to the stagnation point; the lift force may become important for small size particles; the gravitational force, the buoyancy, and the added mass force were found negligible for all the simulated flow conditions; the effect of turbulent dispersion must be accounted for (Fig. 9 and Table 4). Being capable in evaluating the resistance encountered by travelling particles taking their shape into account is fundamental, as this feature has a direct impact on the wear estimates (Fig. 10 and Table 5). The use of the Haider and Levenspiel correlation for the drag coefficient (Eq. 3), in which the effect of particle shape is quantified by means of the particle spherical coefficient, is an interesting option, but it requires this parameter to be properly defined. Fully-sharp, semi-rounded, and fully-rounded particles may be attributed a particle spherical coefficient equal to 0.66, 0.76, and 0.86, respectively.

The erosion model has a major impact on the wear estimates, and, at present, none of the tested correlations proved accurate (Figs. 11 and 12 and Table 7). The erosion model by Oka, Okamura, and Yoshida appears the best choice and, furthermore, it has the considerable advantage of depending

solely on quantities which are generally known. Anyway, deviations up to a factor 5 on the integral erosion ratio have to be accounted for, underlining the need for further study regarding the physics of both liquid-particle flows and the impact wear process.

### Acknowledgements

The present work has been supported by ENI S.p.A. through the research contract “Erosion Prediction in Control Operation”

### References

- [1] R.J.K. Wood, T.F. Jones, N.J Miles, J. Ganeshalingam, Upstream swirl-induction for reduction of erosion damage from slurries in pipeline bends, *Wear* 250 (2001) 770778.
- [2] C.T. Crowe, J.D. Schwarzkopf, M. Sommerfeld, Y. Tsuji, *Multiphase flows with droplets and particles*, CRC Press, Boca Raton, US-FL, 2012.
- [3] R.W. Lyczkowski, J.X. Bouillard, State-of-the-art review of erosion modelling in fluid/solid systems, *Prog. En. Comb. Sci.* 28 (2002) 543–602.
- [4] M. Parsi, K. Najmi, F. Najafifard, S. Hassani, B.S. McLaury, S.A. Shirazi, A comprehensive review of solid particle erosion modeling for oil and gas wells and pipelines applications, *J. Nat. Gas Sci. Eng.* 21 (2014) 850–873.

- [5] G.V. Messa, I. Ingrosso, S. Malavasi, A new methodology for erosion prediction using Eulerian-Eulerian CFD models, Proc. ASME Pressure Vessels and Piping Conference, Paper No. PVP2015-45608, 2015.
- [6] G.V. Messa, G. Ferrarese, S. Malavasi, A mixed EulerEuler/Euler-Lagrange approach to erosion prediction, Wear 342-343 (2015) 138–153.
- [7] G.V. Messa, S. Malavasi, A numerical strategy to account for the effect of self-induced geometry changes in wear estimation, Proc. 9th Int. Conf. on Multiphase Flow, Paper No. 133, 2016.
- [8] M.S. Wallace, W.M. Dempster, T. Scanlon, J. Peters, S. McCulloch, Prediction of impact erosion in valve geometries, Wear 256 (2004) 927–936.
- [9] V.B. Nguyen, Q.B. Nguyen, Z.G. Liu, S. Wan, C.Y.H. Lim, Y.W. Zhang, A combined numerical experimental study on the effect of surface evolution on the water sand multiphase flow characteristics and the material erosion behavior, Wear 319 (2014) 96-109.
- [10] V.B. Nguyen, Q.B. Nguyen, Y.W. Zhang, C.Y.H. Lim, B.C. Khoo, Effect of particle size on erosion characteristics, Wear 348-349 (2016) 126–137.
- [11] M.H. Wang, C. Huang, K. Nandakumar, P. Mineev, J. Luo, S. Chiovelli, Computational fluid dynamics modelling and experimental study of erosion in slurry jet flows, Int. J. Comput. Fluid Dyn. 23 (2009) 155–172.
- [12] A. Mansouri, S.A. Shirazi, B.S. McLaury, Experimental and numerical investigation of the effect of viscosity and particle size on the erosion

- damage caused by solid particles, Proc. ASME-FEDSM2014, Paper No. 21613, 2014.
- [13] H.S. Grewal, H. Singh, E.S. Yoon, Interplay between erodent concentration and impingement angle for erosion in dilute water-sand flows, *Wear* 332-333 (2015) 1111–1119.
- [14] S. Turenne, M. Fiset, J. Masounave, The effect of sand concentration on the erosion of materials by a slurry jet, *Wear* 133 (1989) 95–106.
- [15] A. Gnanavelu, N. Kapur, A. Neville, J.F. Flores, N. Ghorbani, A numerical investigation of a geometry independent integrated method to predict erosion rates in slurry erosion, *Wear* 271 (2011) 712–719.
- [16] V.B. Nguyen, Q.B. Nguyen, C.Y.H. Lim, Q.T. Trinh, S. Sankaranarayanan, Y.W. Zhang, M. Gupta, Effect of impact angle and testing time on erosion of stainless steel at higher velocities, *Wear* 321 (2014) 87–93.
- [17] T. Frosell, M. Fripp, E. Gutmark, Investigation of slurry concentration effects on solid particle erosion rate for an impinging jet, *Wear* 342-343 (2015) 33–43.
- [18] A.J. Gant, M.G. Gee, Wear modes in slurry jet erosion of tungsten carbide hardmetals: Their relationship with microstructure and mechanical properties, *Int. J. Ref. Met. Hard Mater.* 49 (2015) 192–202.
- [19] H. Arabnejad, A. Mansouri, S. A. Shirazi, B. S. McLaury, Evaluation of Solid Particle Erosion Equations and Models for Oil and Gas Industry

- Applications, Proc. SPE Annual Technical Conference and Exhibition, Paper SPE-174987-MS, 2015.
- [20] A. Mansouri, M. Mahdavi, S.A. Shirazi, B.S. McLaury, Investigating the effect of sand concentration on erosion rate in slurry flows, Proc. NACE International Corrosion 2015 Conference & Expo, Paper No. 6130, 2015.
- [21] Y. Zhang, E.P. Reuterfors, B.S. McLaury, S.A. Shirazi, E.F. Rybicki, Comparison of computed and measured particle velocities and erosion in water and air flows, *Wear* 263 (2007), 330–338.
- [22] Y. Zhang, B.S. McLaury, S.A. Shirazi, E.F. Rybicki, A two-dimensional mechanistic model for sand erosion prediction including particle impact characteristics, Proc. NACE International Corrosion 2010 Conference & Expo, Paper No. 10378, 2010.
- [23] R. Okita, Y. Zhang, B.S. McLaury, S.A. Shirazi, Experimental and Computational Investigations to Evaluate the Effects of Fluid Viscosity and Particle Size on Erosion Damage, *ASME J. Fluids Eng.* 134 (2012) 061301.
- [24] L. Ma, C. Huang, Y. Xie, J. Jiang, K.Y. Tufa, R. Hui, Z.S. Liu, Modeling of erodent particle trajectories in slurry flow, *Wear* 334-335 (2015) 49–55.
- [25] A. Mansouri, H. Arabnejad, S.A. Shirazi, B.S. McLaury, A combined CFD/experimental methodology for erosion prediction, *Wear* 332-333 (2015) 1090-1097.

- [26] H. Liu, J. Wang, N. Kelson, R.J. Brown, A study of abrasive waterjet characteristics by CFD simulation, *J. Mater. Process. Technol.* 153-154 (2004) 488-493.
- [27] G. Mostofa, K.Y. Kil, A.J. Hwan, Computational fluid analysis of abrasive waterjet cutting head, *J. Mech. Sci. Technol.* 24 (2010) 249-252.
- [28] T. Matsumura, T. Muramatsu, S. Fueki, Abrasive water jet machining of glass with stagnation effect, *CIRP Ann. Manuf. Technol.* 60 (2011) 355-358.
- [29] D.A. Axinte, B. Karpuschewski, M.C. Kong, A.T. Beaucamp, S. Anwar, D. Miller, M. Petzel, High Energy Fluid Jet Machining (HEFJet-Mach): From scientific and technological advances to niche industrial applications, *CIRP Ann. Manuf. Technol.* 63 (2014) 751-771.
- [30] R.H.M. Jafar, H. Nouraei, M. Emamifar, M. Papini, J.K. Spelta, Erosion modeling in abrasive slurry jet micro-machining of brittle materials, *J. Manuf. Process.* 17 (2015) 127-140.
- [31] H.K. Versteeg, W. Malalasekera, *An Introduction to Computational Fluid Dynamics The Finite Volume Method*, Pearson Prentice Hall, Harlow UK, 2007.
- [32] F.R. Menter, Two-equation eddy-viscosity turbulence models for engineering applications, *AIAA J.* 32 (1994) 1958-1605.
- [33] B.E. Launder, D.B. Spalding, The numerical computation of turbulent flows, *Comput. Methods Appl. Mech. Eng.* 3 (1974) 269-289.

- [34] V. Yakhot, S.A. Orszag, S. Thangam, T.B. Gatski, C.G. Speziale, Development of turbulence models for shear flows by a double expansion technique, *Phys. Fluids A* 4 (1992), 1510–1520.
- [35] S.E. Kim, D. Choudhury, A Near-Wall Treatment Using Wall Functions Sensitized to Pressure Gradient. In *ASME FED 217, Separated and Complex Flows*, 1995.
- [36] E. Loth, *Particles, drops and bubbles: Fluid dynamics and numerical methods*, Draft for Cambridge University Press, 2011. Submitted for publication.
- [37] A. Haider, O. Levenspiel, Drag coefficient and terminal velocity of spherical and non-spherical particles, *Powder Technol.* 58 (1989) 63–70.
- [38] R. Mei, An approximate expression for the shear lift force on a spherical particle at finite Reynolds number, *Int. J. Multiphase Flow* 18 (1992) 145–147.
- [39] *ANSYS FLUENT Theory Guide*, ANSYS inc., Southpoint, 275 Technology Drive, Canonburg, PA 15317, USA, 2013.
- [40] Y.I. Oka, K. Okamura, T. Yoshida, Practical estimation of erosion damage caused by solid particle impact. Part 1: Effects of impact parameters on a predictive equation, *Wear* 259 (2005), 95–101.
- [41] Y.I. Oka, T. Yoshida, Practical estimation of erosion damage caused by solid particle impact. Part 2: Mechanical properties of materials directly associated with erosion damage, *Wear* 259 (2005), 102–109.

- [42] H. Arabnejad, A. Mansouri, S.A. Shirazi, B.S. McLaury, Development of mechanistic erosion equation for solid particles, *Wear* 332–333 (2015), 1044–1050.
- [43] DNV-GL, Managing sand production and erosion. Recommended practice DNVGL-RP-O501, Oslo, Norway, 2015.
- [44] C. Huang, S. Chiovelli, P. Minev, J. Luo, K. Nandakumar, A comprehensive phenomenological model for erosion of materials in jet flow, *Powder Technol.* 187 (2008), 273–279.
- [45] H. Schlichting, *Boundary-Layer Theory*, McGraw-Hill, New York, 1960.
- [46] A. Forder, M. Thew, D. Harrison, A numerical investigation of solid particle erosion experienced within oilfield control valves, *Wear* 216 (1998), 184–193.
- [47] T. Grant, W. Tabakoff, Erosion prediction in turbomachinery resulting from environmental solid particles, *J. Aircraft* 12 (1975), 471–547.
- [48] W.C. Yang, *Handbook of fluidization and fluid-particle systems*, Marcel Dekker Inc., New York, 2003.